Technical University of Denmark

DTU

# Direction-of-Arrival Analysis of Airborne Ice Depth Sounder Data

**Nielsen, Ulrik; Yan, Jie-Bang; Gogineni, Sivaprasad; Dall, Jørgen**

[Link back to DTU Orbit](Link back to DTU Orbit)

**DTU Library**
Technical Information Center of Denmark

# Direction-of-Arrival Analysis of Airborne Ice Depth Sounder Data

Ulrik Nielsen, Jie-Bang Yan, *Member, IEEE,*
Sivaprasad Gogineni, *Fellow, IEEE,* and Jørgen Dall, *Member, IEEE*

*Abstract*—In this paper, we analyze the direction of arrival (DOA) of the ice sheet data collected over Jakobshavn Glacier with the airborne Multi-Channel Radar Depth Sounder (MCRDS) during the 2006 field season. We extracted weak ice–bed echoes buried in signals scattered by the rough surface of the fast-flowing Jakobshavn Glacier by analyzing the direction of arrival of signals received with a 5-element receive-antenna array. This allowed us to obtain ice thickness information which is a key parameter when generating bed topography of glaciers. We also estimated ice–bed roughness and bed slope from the combined analysis of the DOA and radar waveforms. The bed slope is about 8 degrees and the roughness in terms of RMS slope is about 16 degrees.

*Index Terms*—Airborne radar, direction-of-arrival (DOA) estimation, glacier, ice sounding, radar remote sensing, surface scattering.

## I. INTRODUCTION

SATELLITE observations show that both the Greenland and Antarctic ice sheets are losing mass [1], [2]. Most of the ice loss is occurring around ice-sheet margins and through fast-flowing glaciers [3]. Although satellites provide much-needed information on ice-surface elevation, surface velocity, and total mass, there is currently no satellite-based sensor that is able to measure ice thickness. Bed topography and basal conditions for areas losing ice are needed to improve ice-sheet models. These models are essential to predicting the response of the ice sheets to a warming climate. One of the key parameters needed is ice sheet thickness, which can be extracted using radar depth sounding techniques [4], [5]. In addition, we are interested in the basal conditions of the ice sheets as they determine the boundary conditions of the ice sheet models. Basal conditions largely impact on the ice flow velocity and therefore precise knowledge of them is especially important for estimation of the mass balance [6].

### A. Multi-phase-center-based Radar Ice Sounding

The weak nadir radar signals from the ice–bed interface are often masked by off-nadir surface clutter, signals scattered from extremely rough crevassed surfaces in ice sheet margins. Synthetic Aperture Radar (SAR) processing can be used to suppress surface clutter in the along-track direction, but it is ineffective in reducing the across-track clutter. Large across-track antenna arrays can be used to obtain a narrow across-track antenna beam to suppress surface clutter in this direction. At the same time, to avoid excessive attenuation of the signals reflected within the ice, radars are normally operated in the VHF part of the electromagnetic spectrum. The long wavelengths in this band require large-antenna dimensions to obtain an antenna beam that is sufficiently narrow to reduce across-track surface clutter. Such large antenna dimensions cannot be accommodated on airborne platforms, and additional clutter suppression is, therefore, needed to compensate for these limitations. The current research in this field is based on multi-channel systems combined with advanced coherent post-processing of data. By using multi-channel-receivers to sample array elements individually, beamforming techniques can be utilized to synthesize adaptive-antenna patterns that suppress the surface clutter from specific off-nadir angles while a high gain is maintained in the nadir direction [7].

### B. DOA Estimation in Radar Ice Sounding

In addition to beamforming, the multi-phase-center systems also provide the opportunity to perform direction-of-arrival (DOA) estimation of the different signal components within the received returns. In relation to ice sounding, early studies on airborne InSAR in [8] can be seen as a precursor to DOA estimation. A ground-based radar configuration was used in [9] to perform actual DOA estimates of the bed return. In [10], DOA data are used as the primary data product to produce swath measurements of both the ice surface and bedrock-topography. This study is the first published work on DOA estimation applied to airborne ice sounding data. The results reported in [10] are based on data acquired by the Multi-Channel Radar Depth Sounder (MCRDS) developed by the Center for Remote Sensing of Ice Sheets (CReSIS) at the University of Kansas (KU). The radar system is in this experiment operated in ping-pong mode to provide 12 effective receive phase centers. Estimation of the DOA angles of the surface clutter and bed return are used to compute relative elevations in slant-range geometry, followed by a mapping

to ground range to obtain the topographic map in Cartesian coordinates. DOA estimation based on data acquired with an upgraded version of the system, MCoRDS/I [11], have been used to support the investigation of the bed topography of more glaciers including Jakobshavn [12].

In [13], DOA estimation has been applied to data acquired with the 4-channel POLarimetric Airborne Radar Ice Sounder (POLARIS) [14] developed by the Technical University of Denmark (DTU), to improve the performance of surface clutter suppression techniques. The DOA angles of the surface clutter are estimated and used to optimize the synthesis of the antenna patterns for improving clutter suppression.

Recently, DOA estimation based on POLARIS data is used to show an along-track variation of the effective scattering center of the surface return caused by a varying penetration depth [15], which directly provides glaciological information.

In this paper we present further applications of the DOA estimation technique for radar ice sounding. We used MCRDS multi-phase-center data collected over Jakobshavn Glacier during the 2006 Greenland field season to convert radar echograms into a DOA representation. With this representation of the radar data we were able to detect some of the most challenging parts of the bed along the channel of the fastest flowing glacier on the earth. A model-based approach was then used to interpret the DOA estimation of the bed return. Further analysis showed that the backscattering characteristics of the ice-bed could be estimated by combining the DOA data and the radar waveform data. Based on the data, the across-track slope of the bed was estimated as a fitted model parameter. Finally, information on the bed roughness in terms of the RMS slope was obtained by forward modelling using the Incoherent Kirchhoff Model (IKM).

### C. Paper Outline

The paper is organized as follows. Section II provides details on the MCRDS system and the associated dataset. A signal model is presented in Section III along with algorithms for DOA estimation. In Section IV the algorithms are applied to data and used to provide an alternative representation based on DOA. This representation is used for detection of the bed in Section V and for retrieval of its backscattering characteristics in Section VI. Finally, in Section VII, we summarize and conclude the paper.

## II. SYSTEM AND DATA DESCRIPTION

MCRDS [16] is a high-sensitivity radar system developed for the collection of ice-sheet data. During the 2006 Greenland field mission, MCRDS was installed on the DHC-6 Twin-Otter aircraft from de Havilland Canada Ltd and was operated at 150 MHz with a bandwidth of 20 MHz. The system was effectively configured with a 10-element antenna array of folded dipoles mounted in the across-track direction. The array was divided into two 5-element sub-arrays installed under each wing, as shown in Fig. 1. The left wing sub-array was used for transmission and the right for reception. All elements in the transmit array were excited with uniform weights during transmission. The pulse length was 10 μs with



Fig. 1. A photography showing the 5-element sub-array of folded dipole elements mounted under the right wing of the Twin-Otter aircraft.
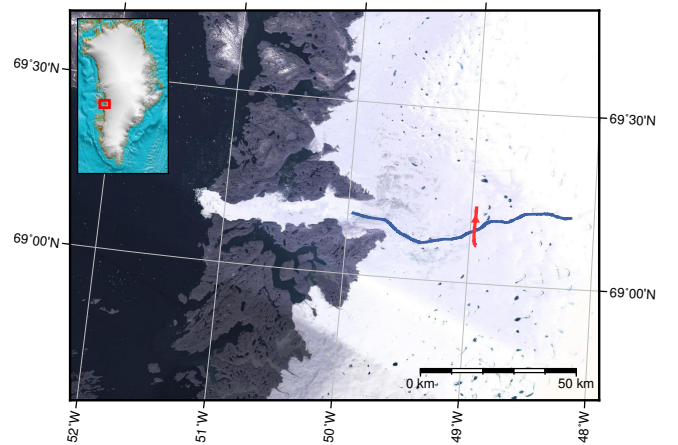


Fig. 2. Flight track (red) over the Jakobshavn Glacier at the west coast of Greenland in the 2006 field season. The blue line corresponds to the location of the glacier channel. The flight track corresponds to frame 5, segment 4 in the dataset acquired May 30, 2006.

a total transmit power of 800 W. A multi-channel receiver was used to sample signals from each receive-antenna element individually. The spacing of the effective phase centers was approximate $0.3\lambda$, where $\lambda$ is the wavelength in free space of the center frequency.

Data acquired with the MCRDS system in 2006 at the Jakobshavn Glacier were used for the DOA analysis. The data were acquired according to the flight track shown in Fig. 2. Results for a segment perpendicular to the ice flow are presented in this paper. The segment was flown northward and is highlighted in red in the figure. The segment represents a strong complex clutter scenario with high attenuation that is difficult to sound. This scenario is well suited for illustrating the capabilities of the proposed methods. The altitude of the flight track is approximate 270 m above the ice surface.

### A. Signal Processing

A linear frequency-modulated chirp was used for transmitted pulses to employ pulse compression. The received data were compressed using a matched filter with a frequency-domain Hanning window to suppress range sidelobes.

SAR processing was used to improve the along-track resolution by synthesizing a long aperture. The frequency-wavenumber (F-K) focusing algorithm that exploits the Fast Fourier Transform (FFT) for computational efficiency was used for processing.

By using pulse compression and SAR processing, a nominal resolution in range and azimuth of 7.5 m (50 ns) and 5 m, respectively, was obtained.

## III. DIRECTION-OF-ARRIVAL ESTIMATION

Several algorithms for DOA estimation exist. They include the well-established MUltiple SIgnal Classification (MUSIC) [17] and Maximum Likelihood (ML) [18] algorithms. Both of these algorithms have super-resolution capabilities and other desirable properties such as statistical consistency and high accuracy in adverse situations such as low SNR scenarios. Due to this as well as their applications in a number of fields, MUSIC and ML are the algorithms chosen for the study in this paper. Within the field of radar ice sounding, the algorithms have previously been applied a few times for different purposes. In [9], MUSIC has been applied to data acquired with a ground-based radar depth sounder configuration, while ML has been applied to data from the airborne experiments in [10], [13], and [15].

We will now briefly describe the array signal model that is the basis for both algorithms.

### A. Signal Model

The signal received at time $t$ by the $N$ array sensors can be expressed in vectorial form as

$$\boldsymbol{x}(t) = \boldsymbol{a}(\theta)s(t) + \boldsymbol{e}(t) \tag{1}$$

where $\boldsymbol{x}(t)$ is an $N \times 1$ vector, $s(t)$ is the complex echo signal at a reference sensor, $\boldsymbol{e}(t)$ is an additive Gaussian noise component, and $\boldsymbol{a}(\theta)$ is the so-called array transfer vector (or steering vector). This vector describes the phase shift at each of the sensors corresponding to the inter-element time delays determined by the array geometry and the given DOA, $\theta$:

$$\boldsymbol{a}(\theta) = \begin{bmatrix} H_1(\theta)e^{-j\omega_c\tau_1} & \dots & H_N(\theta)e^{-j\omega_c\tau_N} \end{bmatrix}^{\mathrm{T}} \tag{2}$$

where $(\cdot)^{\mathrm{T}}$ is the transpose operator, $\omega_c$ is center angular frequency, and $\tau_n$ is the time delay at the $n$th sensor relative to an arbitrary reference sensor. Equation (2) also takes into account the sensor transfer functions, $H_n(\theta)$.

By applying the superposition principle to (1), $Q$ simultaneously received echo signals with different DOA can be described in the following way

$$\boldsymbol{x}(t) = \boldsymbol{A}(\boldsymbol{\Theta})\boldsymbol{s}(t) + \boldsymbol{e}(t) \tag{3}$$

where

$$\boldsymbol{A}(\boldsymbol{\Theta}) = [\boldsymbol{a}(\theta_1) \ \dots \ \boldsymbol{a}(\theta_Q)] \tag{4}$$

is the $N \times Q$ steering matrix formed by column-wise concatenation of the steering vectors corresponding to each of the $Q$ signals, and $\boldsymbol{s}(t)$ is a vector collecting the $Q$ signal components at time $t$, i.e.,

$$\boldsymbol{s}(t) = [s_1(t) \ \dots \ s_Q(t)]^{\mathrm{T}}. \tag{5}$$

The steering matrix $\boldsymbol{A}$ is a function of the DOA vector $\boldsymbol{\Theta}$, which contains the $Q$ DOA angles.

A single time instance of $\boldsymbol{x}$ is denoted a *snapshot*. A collection of $M$ snapshots acquired at time instances $t_1, \dots, t_m$ can be modelled as

$$\boldsymbol{X} = \boldsymbol{A}(\boldsymbol{\Theta})\boldsymbol{S} + \boldsymbol{E} \tag{6}$$

where $\boldsymbol{X}$ and $\boldsymbol{E}$ are $N \times M$ matrices, $\boldsymbol{A}$ is $N \times Q$, and $\boldsymbol{S}$ is $Q \times M$. Each column in $\boldsymbol{X}$, $\boldsymbol{S}$, and $\boldsymbol{E}$ corresponds to a specific snapshot. For further details regarding the signal model see [10], [19].

Before we move on to a review of MUSIC and ML, we first define the sample covariance matrix as

$$\boldsymbol{R} = \frac{1}{M} \sum_{m=1}^{M} \tilde{\boldsymbol{x}}(t_m)\tilde{\boldsymbol{x}}^{\mathrm{H}}(t_m). \tag{7}$$

where $(\cdot)^{\mathrm{H}}$ is the Hermitian transpose and $\tilde{\boldsymbol{x}}$ is a measured array sample corresponding to the signal model from (3). In this way, the covariance matrix is estimated as an average over a given set of snapshots. In this paper, the snapshots are extracted as a number of consecutive samples in azimuth—all at the same given range gate.

### B. Multiple Signals Classification (MUSIC)

MUSIC exploits the eigen-decomposition of $\boldsymbol{R}$, i.e.,

$$\boldsymbol{R} = \boldsymbol{U}\boldsymbol{\Lambda}\boldsymbol{U}^{\mathrm{H}} \tag{8}$$

where $\boldsymbol{\Lambda}$ is a diagonal matrix containing the $N$ eigenvalues of $\boldsymbol{R}$, and $\boldsymbol{U}$ is an orthonormal basis consisting of the corresponding eigenvectors.

The DOA estimates are determined as the $Q$ highest peaks of the so-called MUSIC-spectrum [17] given by

$$P_{\mathrm{MU}}(\theta) = \frac{1}{\boldsymbol{a}^{\mathrm{H}}(\theta)\boldsymbol{U}_n\boldsymbol{U}_n^{\mathrm{H}}\boldsymbol{a}(\theta)} \tag{9}$$

where $\boldsymbol{U}_n$ is the subset of eigenvectors in $\boldsymbol{U}$ that corresponds to the $N - Q$ smallest eigenvalues. The subspace spanned by $\boldsymbol{U}_n$ is known as the noise subspace.

### C. Maximum Likelihood (ML)

The ML solution [18] of the DOA vector can be expressed as

$$\boldsymbol{\Theta}_{\mathrm{ML}} = \min_{\boldsymbol{\Theta}} \mathrm{tr} \Big[ \boldsymbol{A}(\boldsymbol{\Theta}) \big( \boldsymbol{A}^{\mathrm{H}}(\boldsymbol{\Theta})\boldsymbol{A}(\boldsymbol{\Theta}) \big)^{-1} \boldsymbol{A}^{\mathrm{H}}(\boldsymbol{\Theta})\boldsymbol{R} \Big] \tag{10}$$

where $\mathrm{tr}[\cdot]$ is the trace of the bracketed matrix. The ML estimator with the assumption of $Q$ signal components involve a computationally-intensive $Q$-dimensional search. The computation time can be reduced by applying the alternating projection algorithm [18] based on alternating maximization, which transforms the optimization problem into a sequence of much faster one-dimensional searches. The alternating projection algorithm is a suboptimal approach due to nonexhaustive nature of the search. However, except for the lowest signal-to-interference-plus-noise ratio cases the global optimum is almost always found.
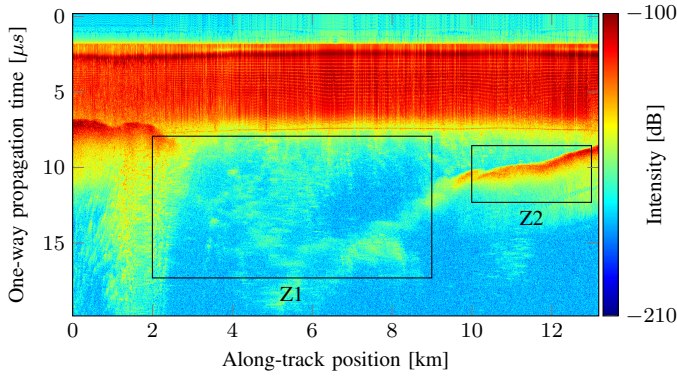
Fig. 3. Echogram based on coherently averaging of the receive channels. The black rectangles show regions of interest: glacier channel (Z1) and bedrock (Z2).

## IV. DOA REPRESENTATION OF RADAR ECHOGRAMS

Now we will utilize the DOA algorithms to obtain an alternative representation of the radar data. Consider the intensity echogram in Fig. 3, which generated by coherently averaging data from all receive channels. The DOA is estimated for each pixel in the echogram. The number of signal components to be estimated can be difficult to determine for the individual pixels. For this reason, and to simplify the processing and interpretation, the number of signal components are assumed to be one for all pixels, i.e. $Q = 1$, even though this is incorrect for some regions of the image. When this assumption does not hold, the DOA of the dominating signal component tends to be the one estimated, and in this way the estimate is still meaningful.

By presenting the DOA estimates as an image with the pixel color representing the DOA angle, the procedure can be considered as a DOA representation of the echogram. The DOA representation of the echogram from Fig. 3 can be seen in Fig. 4 and Fig. 5 using MUSIC and ML respectively. The colormap is thresholded at $\pm 40°$ as indicated by the colorbars. The covariance matrix is estimated based on 5 snapshots, and the DOA images are filtered using a $5 \times 5$ median filter to reduce noise and outliers. A low number of snapshots is chosen in order to ensure statistical stationarity in the rapidly changing scene.

The array manifold, i.e. the set of steering vectors for the DOA interval of interest, is obtained from a full-wave electromagnetic simulation of the combined computer model of the antenna elements and the aircraft according to a similar procedure described in [20].

The outputs of the two algorithms are similar with respect to the large-scale content. The DOA of the near-range pixels are estimated with small (numerical) values, while the DOA of the far-range pixels is large. Dark blue and dark red represent far off-nadir signals while green represents near-nadir returns. Parts of the ice–bed interface can be detected as an abrupt transition from large to small estimated DOA angles, where the dominating signal component changes from off-nadir surface clutter or noise, to the first (near-nadir) return from the bedrock. With respect to the small scale content, the MUSIC images are much noisier compared to the ML image.
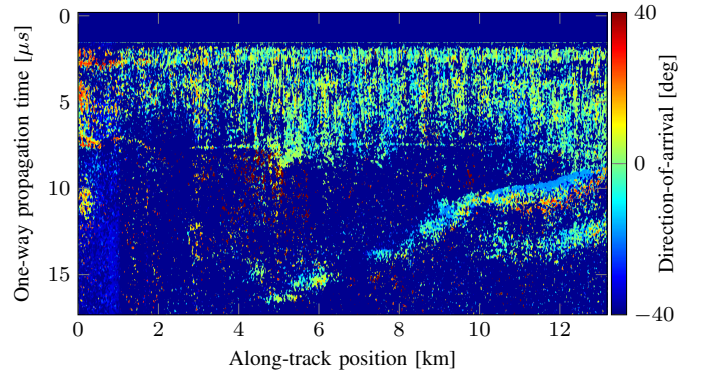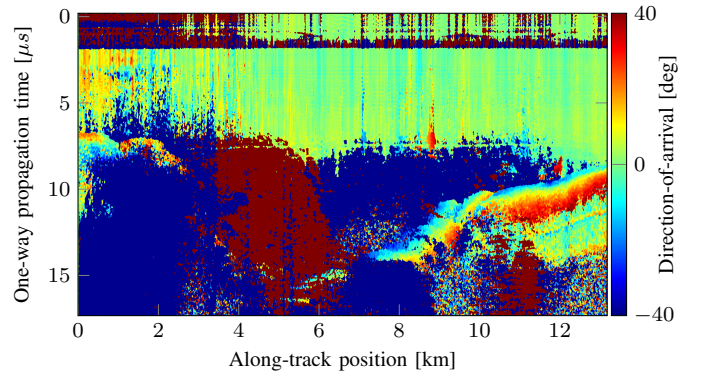


Fig. 4. MUSIC-based DOA image.



Fig. 5. ML-based DOA image.

Furthermore, the ML image reveals large areas of off-nadir surface clutter (dark red) that appears due to a change of sign in DOA angle compared to the background. The transition from ice to bedrock is much more significant in the ML image. In both images, a distinctive color sweep-pattern in the estimated DOA angle is seen right after the first bed return. Again, the phenomenon is more pronounced in the ML image. Based on this visual comparison of the MUSIC image and the ML image, we conclude that the ML algorithm for this specific scene and clutter scenario is preferable for the further analysis.

The next two sections address observations in the DOA representation in terms of the detectability of the ice–bed interface, and the sweep-pattern in the estimated DOA angle at the bed.

## V. ICE BED DETECTION

By examining the echogram in Fig. 3, we can see that the subsurface returns are highly contaminated by surface clutter. The bedrock is detectable at the beginning and end of the frame (left/right of the glacier channel), but at the middle section (glacier channel), the weak bed return cannot be discriminated from the clutter. Therefore, detection of the bed is not possible which is unfortunate since this data product and its derivatives are essential in glaciological modelling.

The MVDR beamformer can be used to reduce the surface clutter in the echogram. An echogram based on MVDR processing is shown in Fig. 6. When comparing with Fig. 3 it
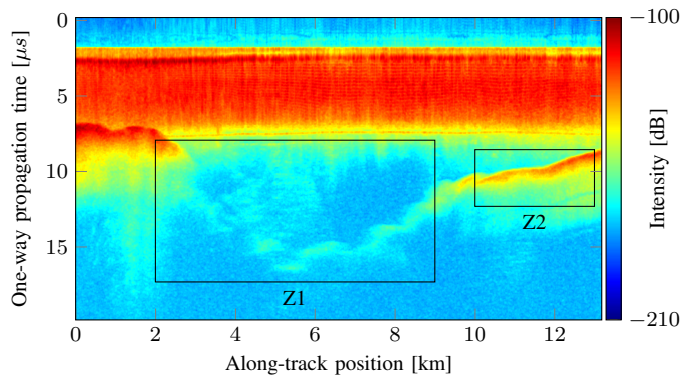
Fig. 6. Echogram based on MVDR processing where 11 snapshots are used for estimation of the covariance matrix. A $5 \times 5$ mean filter is applied.
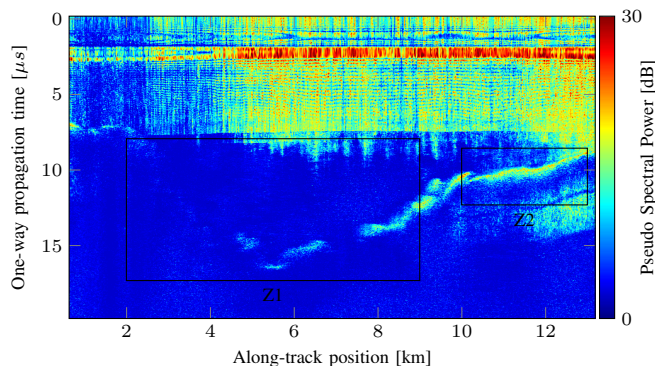


Fig. 7. MUSIC pseudo-spectral power derived image.

is seen that the bed is more distinctive but that surface clutter is still limiting the detectability. As an alternative to MVDR, a similar visualization can be derived from the MUSIC-spectrum in (9), as presented in [12]. For comparison, a MUSIC pseudo-spectral power derived image from [21] is shown in Fig. 7.

Now we consider the ML DOA representation for bed detection. In Fig. 8, enlargements of the glacier channel in the echograms, MUSIC image, and DOA image are stacked for easy comparison. The colormaps of the enlarged images are scaled to enhance the local features. A $5 \times 5$ mean filter is applied to the intensity images.

It is seen that the bed signal can be discriminated from the clutter in the DOA image, which is not possible in the standard radar-intensity echogram. The bed is more distinctive in the MVDR echogram compared to the standard echogram but detection is a challenge in the strong clutter region. A high amount of strong clutter is suppressed in the MUSIC image. However, the weak parts of the remaining bed signal is hard to distinguish from the background noise.

For the DOA image, on the other hand, even though the bed signal is flickering in the strong clutter region, the coverage is sufficient to perform a reasonable trace of the interface with only a minor deviation at 8 km, as illustrated in Fig. 9. The tracing is done by scanning each line through range until a significant discontinuity from off-nadir to near-nadir is detected. This procedure corresponds to a tracing of the signal change from volume clutter to base return. In the case
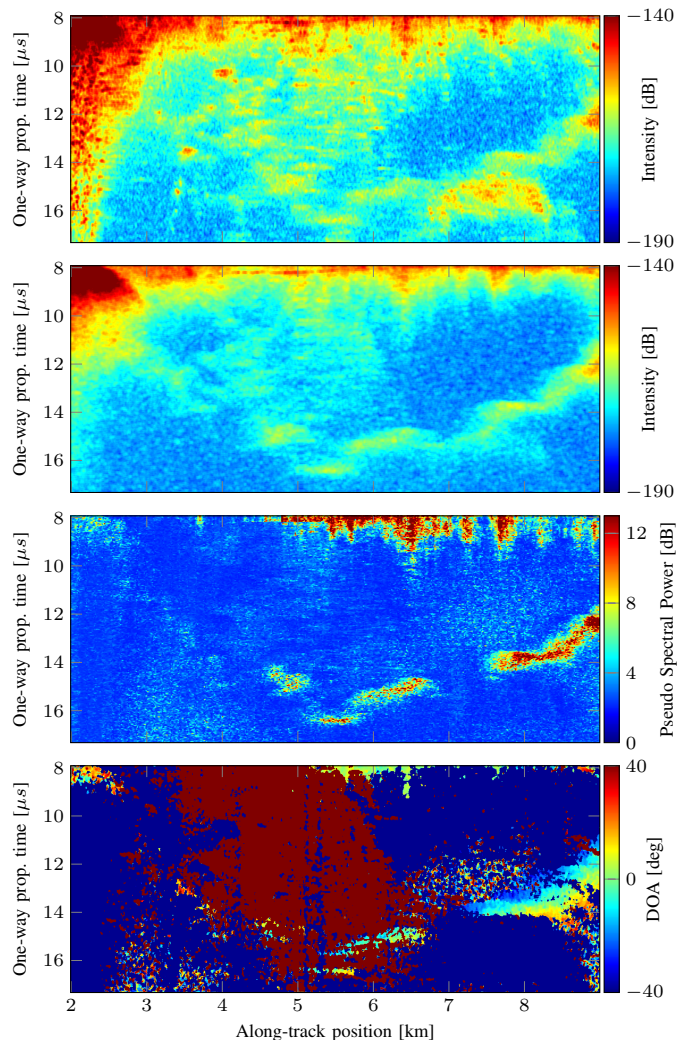


Fig. 8. Enlargement (Z1) of glacier channel, standard echogram (first), MVDR processed echogram (second), MUSIC pseudo-spectral power derivative (third), and ML DOA image (fourth).

where multiple basal targets are present at a given along-track position, the one closest to the radar is implicitly traced. In the strong clutter region, the detection might be based only on a few pixels in range. The trace is interpolated at lines where no bed signal is present at all.

In this way the DOA image can be a powerful representation for discrimination and visualization of different types of targets, which can be used to interpret the echogram or for direct applications such as bed detection.

## VI. ICE BED BACKSCATTERING CHARACTERISTICS ESTIMATION

Estimating surface roughness parameters from backscatter is a well-known technique. However, the topography impacts the local incidence angle, and when it comes to estimation of surface roughness of glaciated bedrock, the ice complicates the problem by causing refraction and attenuation of the electromagnetic waves. In the following we present a method for estimation of bed roughness. The method is based on the DOA representation of the data that allows us to compensate
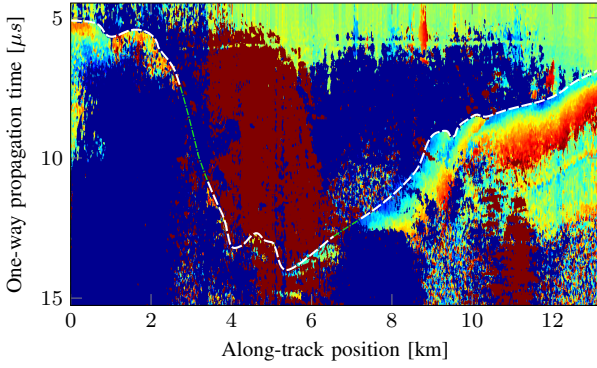
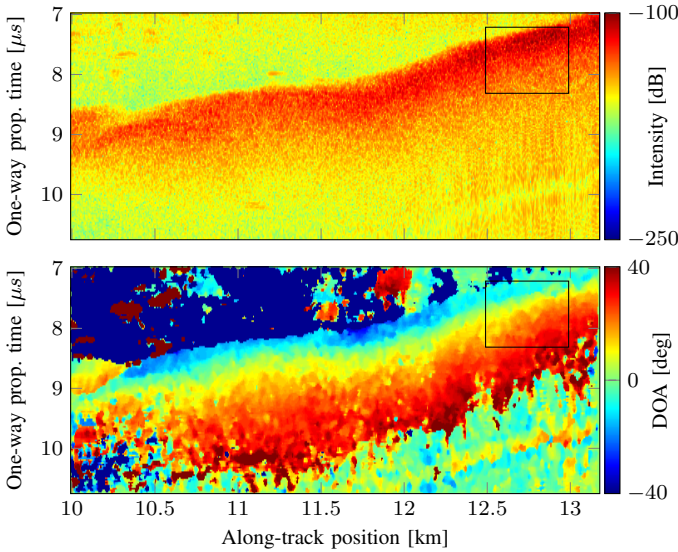Fig. 9. Bed detection (white, dashed) with interpolation (green, dot-dashed); based on the ML DOA image.



Fig. 10. Enlargement (Z2) of the bed, echogram (top) and ML DOA image (bottom).



Fig. 11. Geometry and notation associated with illumination of sloped (across-track) bed at different range gates.

for the bed topography, and the resulting change of incidence angle, refraction and attenuation.

We start out by analysing the DOA sweep-pattern observed near the bed. An enlargement containing a part of the bed is shown in Fig. 10. A sub-image for further analysis is marked in the figure. The following analysis suggests that the DOA pattern represents an off-nadir return from a rough sloped bed.

The sounding geometry with notation associated with a sloped (across-track) bed is illustrated in Fig. 11. Since the data are Doppler processed in the along-track direction, the along-track extent of the resolution cell is small. In this way, the extent of the resolution cell is (pulse) limited to the across-track direction at zero Doppler. At $t_0$ the first bed return is reflected corresponding to the shortest electrical distance from the radar to the bed. The DOA of this first bed return, corrected through the Snell's law of refraction at the air–ice interface, corresponds to the refraction angle $\phi$ of the shortest ray path $s_i$, which corresponds to the across-track slope of the bed. Later time, i.e. at $t_1, t_2, \ldots$, two signals are reflected corresponding to the left-hand side (LHS) and right-hand side (RHS) intersections of the wavefront with the ice–
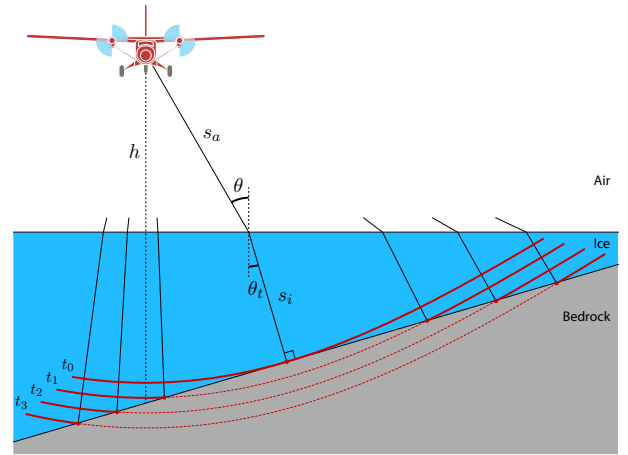
bed interface, as illustrated in the figure. It should be noted that when referring to one of these two components, a specific point on the bed can be described by either range, DOA, or (propagation) time. Therefore, the representations should be read as being ambiguous or interchangeable if either the LHS or RHS intersection is considered. A rough ice–bed interface is assumed such that energy is scattered back towards the radar.

The across-track slope, $\phi(t_0)$, and depth, $s_i(t_0)$, of the bed is estimated using radar and DOA data for the boxed region in Fig. 10. Based on these parameters, a DOA simulation for a flat sloped bed is conducted. The simulation is based on that the leading or trailing edge of the wave are characterized by a constant electrical distance

$$s_a + n s_i = ct, \tag{11}$$

where $c$ is the speed of light in vacuum and $n$ is the refractive index of ice. This combined with Snell's law of refraction,

$$\sin \theta = n \sin \phi, \tag{12}$$

is used to describe the wave within the ice. By specifying the altitude $h = s_a \sin \theta$, and the depth and across-track slope of the bed, the DOA signal $\phi(t)$ for the bed return can be simulated.

The DOA estimate of the boxed region in Fig. 10 is averaged in the along-track direction to a single line and plotted with the simulation as a function of time in Fig. 12.

The simulation consists of an approximately symmetric two-legged curve, where each leg corresponds to the LHS and RHS bed signal, respectively. It is seen that the estimate and simulation fits very well, but clearly only one of the two components is estimated by the DOA algorithm. The reason for this is that a one-signal ($Q = 1$) ML estimation was performed. In this case, the leg that is centered around nadir is the one estimated because of the transmit antenna pattern. Since the pattern is directed towards nadir, the given signal component is the one dominating the combined signal, hence the one estimated by the DOA algorithm. At a less sloped part of the bed, it was possible with a two-signal estimation to recover both of the signal components from the bed, as seen in
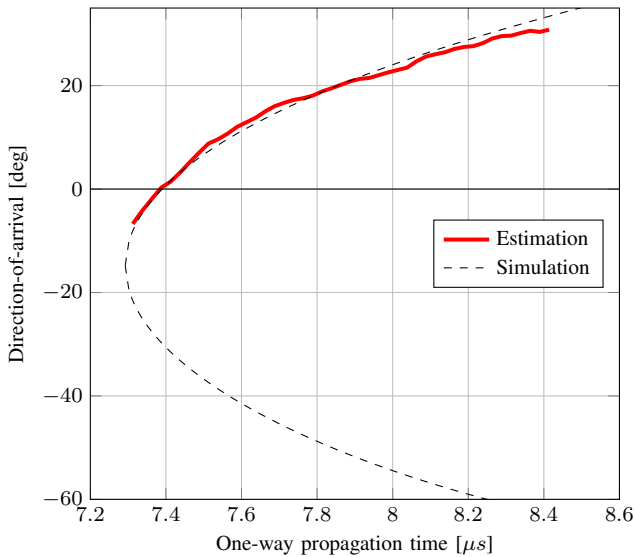
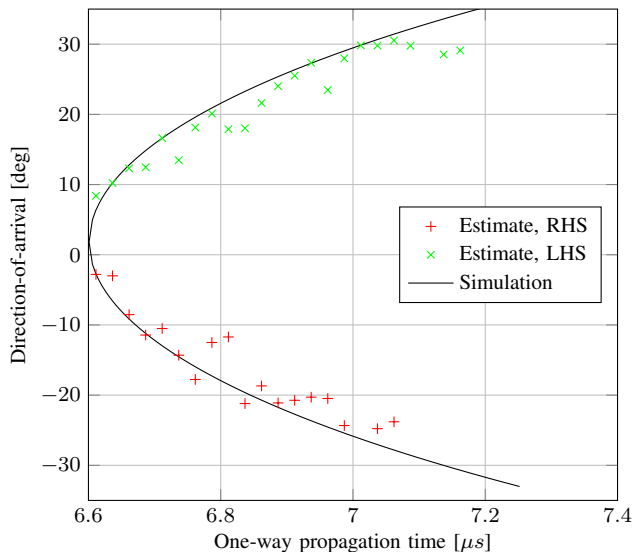Fig. 12. DOA estimation of the bed return along with a simulation based on the geometric model from Fig. 11.

Fig. 13. Two-signal ML DOA estimation and simulation of bed return.

Fig. 13. In the case of a small slope, the geometry is symmetric which results in bed signals of equal amplitude. The retrieval of both bed signals in the low slope scenario strengthens the hypothesis of the bed reflections being the mechanism behind the sweep-pattern.

The case of a single dominating bed signal combined with the DOA information makes it possible to estimate the backscattering characteristics of the bed for a range of incidence angles. This is done by combining the intensity waveform with the corresponding DOA estimate. However, the backscattering information contained in the waveform is affected by several factors such as a varying propagation distance, antenna patterns, refraction at the air–ice interface etc. These factors need to be taken into account to get an accurate estimate of the bed characteristics. In the following section, we will describe a procedure for estimating the backscattering
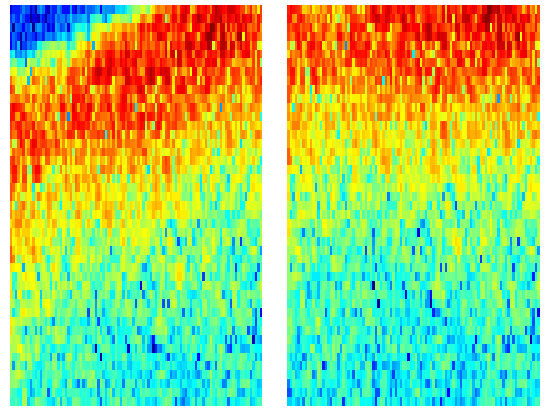
Fig. 14. Illustration of the detrending procedure. Original echogram (left) and the corresponding detrended output (right).

pattern of the bed, which includes corrections of the intensity waveform.

### A. Detrending

We are still considering the data region marked in Fig. 10. To get an accurate estimate of the DOA trace and the waveform of the bed return, both the DOA data and the intensity radar data are averaged in the along-track direction. However, the bed has an along-track slope, which distorts the shape of the DOA trace and the waveform when the data are averaged. In order to avoid this distortion, the data are detrended with respect to the along-track slope before averaging. This is done by tracing the leading edge of the waveform and shifting each line in range accordingly. The procedure is equivalent to averaging in the surface parallel direction and is illustrated in Fig. 14. The resulting DOA trace and waveform after averaging are plotted as a function of time in Fig. 15.

### B. Fitting of Bed Model

To correct for attenuation and refraction at the air–ice interface etc., the geometric model in Fig. 11 is adopted. The model is fitted to the data shown in Fig. 15. As illustrated in the figure with the vertical dashed lines, the data are clipped in the range direction to capture the trailing edge of the waveform and the valid part of the DOA trace. The bed model is now fitted to the data by adjusting the slope parameter $\phi$ and the propagation time corresponding to the closest approach. The error, which is minimized, is evaluated in the DOA representation corresponding to the difference between the data and the model in Fig. 12. The across-track slope of the bed is estimated by the fitted parameter to $\phi = 8°$, which for the specific flight segment corresponds to the slope of the glacier channel.

### C. Waveform Correction

The data are now corrected for four mechanisms:
1) Receive gain
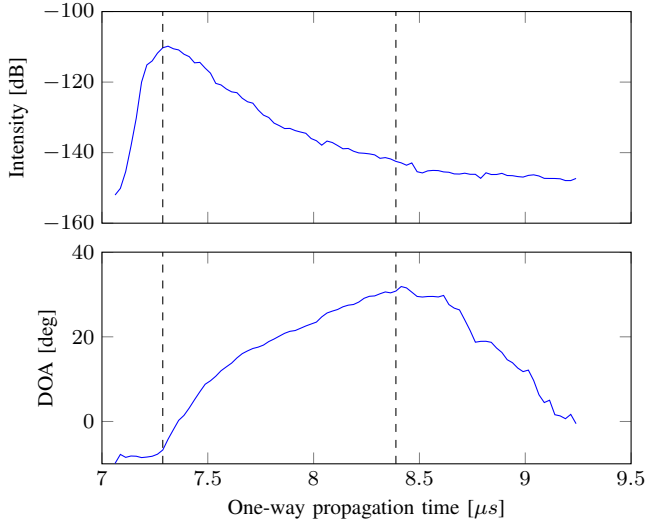2) Transmit gain
3) Attenuation loss
4) Geometric spreading

Fig. 15.   Along-track averaged waveform of the bed return (top) and the correspondingly averaged DOA estimate (bottom).



Fig. 16.   Transmit pattern in the across-track direction, based on a HFSS-simulation of the array manifold.

*1) Receive Gain:* To improve the signal-to-clutter ratio, suppress clutter and the secondary bed return, beamforming is used to steer the receive-beam towards the direction of the dominating bed return.

The output $y$ of beamforming formulated as a spatial filtering process is given by

$$y = \boldsymbol{h}^{\mathrm{H}} \boldsymbol{x}, \tag{13}$$

where $\boldsymbol{h}$ is the $N \times 1$ filter weight vector. In the case of beamsteering, the filter weights are given by [19]

$$\boldsymbol{h} = \frac{\boldsymbol{a}(\theta)}{\boldsymbol{a}^{\mathrm{H}}(\theta)\boldsymbol{a}(\theta)}, \tag{14}$$

where $\theta$ represents the steering angle. The normalization ensures unity gain in the $\theta$-direction, and the correction for the receive gain is in this way incorporated into the filtering process.

DOA data are simulated based on the fitted model and are used as the steering angle in (14). A range varying beam is in this way synthesized for, and applied to, each azimuth line. The filtered data are then detected, detrended, and averaged according to the procedure described earlier.

*2) Transmit Gain:* All transmit elements are used for transmission without any tapering. The resulting transmit pattern is shown in Fig. 16. By using the estimated DOA data in combination with the pattern, the waveform can be corrected for the antenna transmit gain. The antenna pattern is based on simulations [20] and does not take dynamic factors such as wing flexure and vibration into account. This affects the true pattern particularly regarding the depth of the nulls. Furthermore, energy from the secondary bed return and from surface and volume clutter contributes to the received signal, which smoothens the waveform when the transmit gain towards the bed is low. Therefore, if the waveform is corrected with the unmodified simulated pattern with deep nulls, high amplification of the clutter will occur at angles corresponding to the nulls. To avoid this clutter amplification, the nulls of the
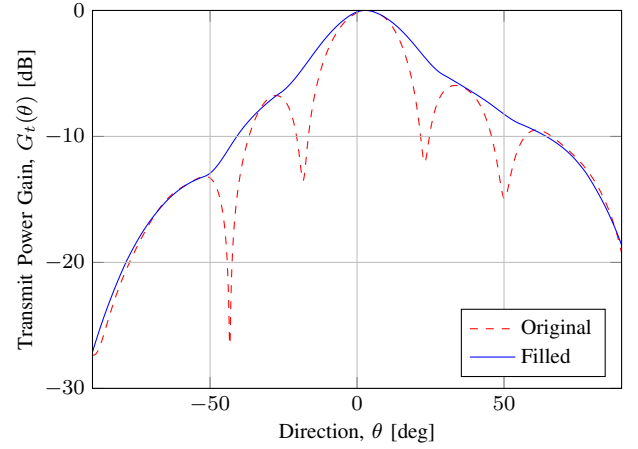
pattern are filled before the correction is applied. The modified transmit pattern is shown in blue in Fig. 16.

*3) Attenuation Loss:* The electromagnetic propagation within the ice involves attenuation losses due to absorption and internal scattering. It is seen from the geometry in Fig. 11 that the propagation distance in ice ($s_i$) for the bed return varies with DOA. When the attenuation coefficient is assumed constant, the attenuation loss is exponentially proportional to the propagated distance in ice, i.e.

$$L_A \propto 10^{a s_i}, \tag{15}$$

where $a$ is the attenuation constant. The attenuation loss varies with DOA through $s_i$, and can be taken into account. Under the assumption of a constant ice temperature and by using the model, $s_i$ is calculated as a function of range and the waveform is corrected accordingly.

*4) Geometric Spreading:* The inverse-square law and the two-way propagation of the pulse result in the geometric spreading loss factor that is related to range in the following way

$$L_{GS} \propto R^4. \tag{16}$$

When $s_a$ is the propagated distance in air, the range is defined as $R = s_a + s_i$ which takes the refraction at the air–ice interface into account. As for the attenuation loss, the geometric model is used to calculate the range for each sample, and the data are corrected accordingly.

*5) Refraction Gain:* Due to refraction at the air–ice interface adjacent rays of a transmitted wave are focused into a smaller area compared to a corresponding free-space scenario. This results in a gain factor known as the refraction gain [22]. Simulations for the geometry of the given scenario show that the variation of the refraction gain can be neglected within the range of DOA angles under consideration. Based on this, no correction of the refraction gain is applied to the data.
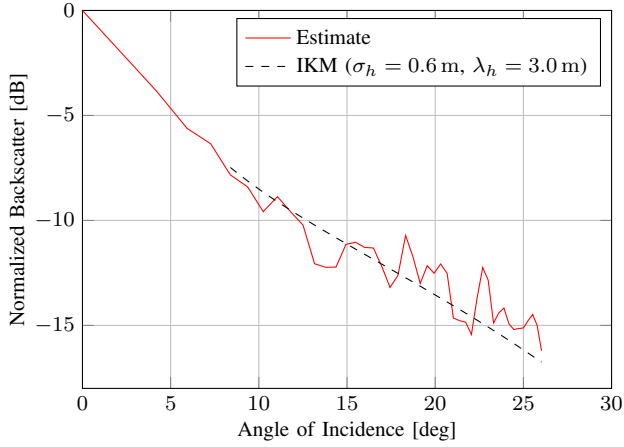
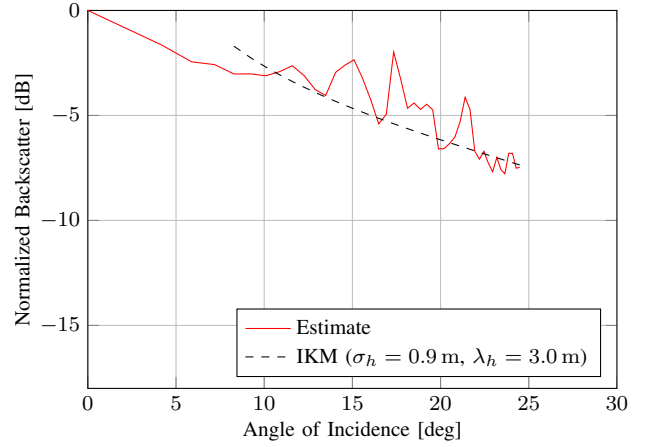Fig. 17. Estimated and simulated backscattering pattern of the bed surface.



Fig. 18. Backscattering pattern of the bed surface as in Fig. 17 but calculated with the assumption of a bed slope equal to zero.

### D. Backscattering Pattern

The corrected waveform that represents backscatter from the bed surface can be expressed as

$$\sigma(\theta) = K \frac{P_{\text{BS}}(\theta) 10^{as_i} R^4}{G_t(\theta)} \tag{17}$$

where $P_{\text{BS}}(\theta)$ is the received power using beamsteering, and $K$ is a product of factors independent of DOA such as the system gain etc. The normalized backscatter is computed by dividing with the backscatter at zero incidence, i.e.

$$\hat{\sigma}(\theta) = \frac{\sigma(\theta)}{\sigma(\theta_0)} \tag{18}$$

where $\theta_0$ is the DOA angle corresponding to zero incidence at the bed, i.e. $t = t_0$ in Fig. 11. Based on the model, the angle of incidence at the bed is calculated from the refracted angle $\phi$ and the estimated bed slope. The normalized backscatter as a function of incidence angle is plotted in Fig. 17.

With the assumption of a random surface with a Gaussian height distribution, the IKM [23][24] is used to model the backscattering coefficient:

$$\sigma_{\text{IKM}}^0(\alpha) = \frac{\Gamma}{2m_s^2 \cos^4 \alpha} \exp\left(-\frac{\tan^2 \alpha}{2m_s^2}\right) \tag{19}$$

where $\alpha$ is the angle of incidence, $\Gamma$ is the Fresnel reflectivity [25] evaluated at normal incidence, and $m_s$ is the root mean square (RMS) slope of the surface given by [24]

$$m_s = \frac{\sqrt{2}\sigma_h}{\lambda_h}. \tag{20}$$

The parameters $\lambda_h$ and $\sigma_h$ are the surface correlation length and RMS height, respectively. The IKM only depends on the RMS slope and is therefore invariant with respect to a common scaling of $\lambda_h$ and $\sigma_h$ as long as the validity conditions [23] are fulfilled. When the surface height variation is Gaussian distributed, the validity conditions are given by [23]

$$k\lambda_h > 6, \tag{21}$$

$$\lambda_h^2 > 2.76\sigma_h\lambda. \tag{22}$$

Furthermore, application of Geometric Optics (Stationary-Phase Approximation) requires that [23]

$$(2k\sigma_h \cos \alpha)^2 > 10. \tag{23}$$

For ice with a relative permittivity of 3.2, $\lambda = 1.12\,\text{m}$ and $k = 5.62\,\text{m}^{-1}$.

The backscatter is obtained by multiplying the coefficient with the time-varying illuminated area, which is calculated based on the fitted geometric model. Since the illuminated area is rapidly changing for small incidence angles, backscatter is only modeled for larger angles, where the estimate of the area is more accurate and robust. The IKM is fitted to the estimated data and is included in Fig. 17. A relative permittivity for ice equal to 3.2 is assumed. The bedrock permittivity enters the model only through the Fresnel reflectivity that appears as a factor in the IKM, (19). Since the IKM is fitted to normalized data, (18), the estimated RMS slope does not depend on the bedrock permittivity. Based on the fit of the IKM, the RMS slope is estimated to 0.28 or 16°, which represents a measure of the bed roughness. For comparison, a recent study [26] estimates bed RMS slopes of Thwaites Glacier in West Antarctica based on radar ice sounding, but with a different surface model and data acquired at a different frequency, which is sensitive to another roughness scale. The slopes are estimated to be between 6° and 8°.

A solid validation of the estimated RMS slope is difficult since direct in situ measurements of the RMS slope cannot be obtained. Processing of different segments will not significantly improve the validation since the roughness can vary with location.

A simulation has been conducted to illustrate the importance of including DOA information for estimation of the bed roughness. The procedure including all waveform corrections used to produce Fig. 17 is repeated except that the bed slope is set to zero. The estimated backscattering pattern and the fitted IKM is shown in Fig. 18. The estimated RMS slope is 0.42 or 24° which differs significantly from the result estimated utilizing DOA information to take the bed slope into account.

## VII. Conclusion

Alternative applications of DOA estimation in relation to airborne radar ice sounding are presented in this paper. We use the MUSIC and ML estimators to convert the radar data into a DOA representation, where the latter is seen to provide superior performance. The DOA representation offers a better visualization of the desired signals and clutter. Based on this we are able to discriminate the desired bed return from strong surface clutter in the channel of the challenging Jakobshavn Glacier. We show how this can be used to detect some of the most challenging parts of the bed along the channel.

Furthermore, a geometric model is used to show how the across-track slope of the bed is related to the DOA pattern of the bed return. In a low slope scenario where the associated geometry gives rise to comparable amplitudes of the LHS and RHS bed signals, the DOA for both components is retrieved and validated with the model. For larger slopes, it is shown that the bed component received closest to nadir is dominant due to amplification caused by the combination of the transmit pattern and asymmetric geometry. This is exploited to retrieve bed characteristics by combining DOA data and waveforms of the radar data. By fitting the geometric model to the data, the across-track slope is estimated. Based on the model, a number of corrections are applied to the waveform to retrieve the received backscatter of the bed surface as a function of the local incidence angle. The backscattering pattern holds information on the bed roughness. To further quantify the roughness, the IKM is fitted to the data and used to estimate a 16° RMS slope of the surface.

## References

[1] E. Rignot, I. Velicogna, M. R. van den Broeke, A. Monaghan, and J. T. M. Lenaerts, "Acceleration of the contribution of the Greenland and Antarctic ice sheets to sea level rise," *Geophys. Res. Lett.*, vol. 38, no. 5, p. L05503, Mar. 2011.

[2] A. Shepherd *et al.*, "A Reconciled Estimate of Ice-Sheet Mass Balance," *Science*, vol. 338, no. 6111, pp. 1183–1189, Nov. 2012.

[3] E. Rignot, J. Mouginot, M. Morlighem, H. Seroussi, and B. Scheuchl, "Widespread, rapid grounding line retreat of pine island, thwaites, smith, and kohler glaciers, west antarctica, from 1992 to 2011," *Geophys. Res. Lett.*, vol. 41, no. 10, pp. 3502–3509, May 2014.

[4] S. Gogineni *et al.*, "Coherent radar ice thickness measurements over the Greenland ice sheet," *Journal of Geophysical Research: Atmospheres*, vol. 106, no. D24, pp. 33 761–33 772, Dec. 2001.

[5] J. Dall *et al.*, "P-band radar ice sounding in Antarctica," in *Proc. IGARSS'12*, Munich, Germany, Jul. 2012, pp. 1561–1564.

[6] M. Schäfer *et al.*, "Sensitivity of basal conditions in an inverse model: Vestfonna ice cap, Nordaustlandet/Svalbard," *The Cryosphere*, vol. 6, no. 4, pp. 771–783, 2012.

[7] J. Li *et al.*, "High-Altitude Radar Measurements of Ice Thickness Over the Antarctic and Greenland Ice Sheets as a Part of Operation IceBridge," *IEEE Trans. Geosci. Remote Sens.*, vol. 51, no. 2, pp. 742–754, Feb. 2013.

[8] J. J. Legarsky, "Synthetic-aperture Radar (SAR) Processing of Glacial-ice Depth-sounding Data, Ka-band Backscattering Measurements and Applications," Ph.D. dissertation, Univ. of Kansas, Lawrence, Kansas, USA, 1999.

[9] J. Paden, T. Akins, D. Dunson, C. Allen, and P. Gogineni, "Ice-sheet bed 3-D tomography," *Journal of Glaciology*, vol. 56, no. 195, pp. 3–11, 2010.

[10] X. Wu, K. C. Jezek, E. Rodriguez, S. Gogineni, F. Rodríguez-Morales, and A. Freeman, "Ice Sheet Bed Mapping with Airborne SAR Tomography," *IEEE Trans. Geosci. Remote Sens.*, vol. 49, no. 10, pp. 3791–3802, Oct. 2011.

[11] F. Rodríguez-Morales *et al.*, "Advanced Multifrequency Radar Instrumentation for Polar Research," *IEEE Trans. Geosci. Remote Sens.*, vol. 52, no. 5, pp. 2824–2842, May 2014.

[12] S. Gogineni *et al.*, "Bed topography of Jakobshavn Isbræ, Greenland, and Byrd Glacier, Antarctica," *Journal of Glaciology*, vol. 60, no. 223, pp. 813–833, 2014.

[13] U. Nielsen, J. Dall, A. Kusk, and S. S. Kristensen, "Coherent Surface Clutter Suppression Techniques with Topography Estimation for Multi-Phase-Center Radar Ice Sounding," in *Proc. EUSAR'12*, Nuremberg, Germany, Apr. 2012, pp. 247–250.

[14] J. Dall *et al.*, "ESA's POLarimetric Airborne Radar Ice Sounder (PO-LARIS): design and first results," *IET Radar, Sonar & Navigation*, vol. 4, no. 3, pp. 488–496, 2010.

[15] U. Nielsen and J. Dall, "Direction-of-Arrival Estimation for Radar Ice Sounding Surface Clutter Suppression," *IEEE Trans. Geosci. Remote Sens.*, vol. 53, no. 9, pp. 5170–5179, Sep. 2015.

[16] A. Lohoefener, "Design and Development of a Multi-Channel Radar Depth Sounder," Master's thesis, University of Kansas, Lawrence, KS, USA, Nov. 2006.

[17] R. O. Schmidt, "Multiple Emitter Location and Signal Parameter Estimation," *IEEE Trans. Antennas Propag.*, vol. 34, no. 3, pp. 276–280, Mar. 1986.

[18] I. Ziskind and M. Wax, "Maximum Likelihood Localization of Multiple Sources by Alternating Projection," *IEEE Trans. Acoust., Speech, Signal Process.*, vol. 36, no. 10, pp. 1553–1560, Oct. 1988.

[19] P. Stoica and R. L. Moses, *Introduction to Spectral Analysis*. Prentice Hall, 1997.

[20] J.-B. Yan *et al.*, "Measurements of In-Flight Cross-Track Antenna Patterns of Radar Depth Sounder/Imager," *IEEE Trans. Antennas Propag.*, vol. 60, no. 12, pp. 5669–5678, Dec. 2012.

[21] (2012, Dec.) MUSIC pseudo-spectral power derived images of the Jakobshavn Glacier. Center for Remote Sensing of Ice Sheets. University of Kansas, Lawrence, KS, USA. [Online]. Available: ftp://data.cresis.ku.edu/data/rds/2006_Greenland_TO/CSARP_music/20060530_04

[22] P. Gudmandsen, *Electromagnetic Probing in Geophysics*. Golem Press, 1971, ch. 9, pp. 321–348.

[23] F. T. Ulaby, R. K. Moore, and A. K. Fung, *Microwave Remote Sensing: Active and Passive*. Addison-Wesley, 1982, vol. II.

[24] G. Picardi *et al.*, "Performance and surface scattering models for the Mars Advanced Radar for Subsurface and Ionosphere Sounding (MARSIS)," *Planetary and Space Science*, vol. 52, no. 1-3, pp. 149–156, 2004.

[25] F. T. Ulaby, R. K. Moore, and A. K. Fung, *Microwave Remote Sensing: Active and Passive*. Addison-Wesley, 1981, vol. I.

[26] D. M. Schroeder, D. D. Blankenship, D. A. Young, A. E. Witus, and J. B. Anderson, "Airborne radar sounding evidence for deformable sediments and outcropping bedrock beneath Thwaites Glacier, West Antarctica," *Geophys. Res. Lett.*, vol. 41, no. 20, pp. 7200–7208, Oct. 2014.

**Ulrik Nielsen** received the B.Sc. and M.Sc. degrees in electrical engineering from The Technical University of Denmark, Copenhagen, Denmark, in 2008 and 2011, respectively.

In 2015 he received his Ph.D. degree in array signal processing from the National Space Institute, Technical University of Denmark. During the Ph.D. he worked on synthetic aperture radar (SAR) tomography techniques for radar ice sounding.

Since March 2015, he has been with IHFood A/S developing computer vision technology. His current field of work includes image analysis, machine learning, and statistical modeling.
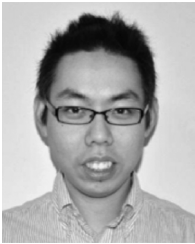
**Jie-Bang Yan** (S'09-M'11) received the B.Eng. (First Class Hons.) degree in electronic and communications engineering from the University of Hong Kong, Hong Kong, in 2006, the M.Phil. degree in electronic and computer engineering from the Hong Kong University of Science and Technology, Hong Kong, in 2008, and the Ph.D. degree in electrical and computer engineering from the University of Illinois at Urbana-Champaign, Champaign, IL, USA, in 2011.

From 2009 to 2011, he was a Croucher Scholar with the University of Illinois at Urbana-Champaign, where he was involved in MIMO and reconfigurable antennas. In 2011, he joined the Center for Remote Sensing of Ice Sheets, University of Kansas, Lawrence, KS, USA, as an Assistant Research Professor. He is currently an Assistant Professor of Electrical and Computer Engineering with the University of Alabama, Tuscaloosa, AL, USA. He holds two U.S. patents and a U.S. patent application related to novel antenna technologies. His current research interests include the design and analysis of antennas and phased arrays, ultrawideband radar systems, radar signal processing, and remote sensing.

Dr. Yan was a recipient of the Best Paper Award in the 2007 IEEE (HK) AP/MTT Postgraduate Conference, the Raj Mittra Outstanding Research Award at IL, USA, in 2011, and the NASA Group Achievement Award in 2013 for the NASA P3 Aircraft Antarctica Mission Team, and was the Best Paper Finalist of the 2015 National Instruments Week. He serves as a Technical Reviewer for several journals and conferences on antennas and remote sensing.

**Sivaprasad Gogineni** (M'84-SM'92-F'99) received the Ph.D. degree in electrical engineering from the University of Kansas (KU), Lawrence, KS, USA, in 1984.

He is currently the Deane E. Ackers Distinguished Professor with the Department of Electrical Engineering and Computer Science, KU, where he is the Director of the NSF Science and Technology with the Center for Remote Sensing of Ice Sheets. He will be joining the University of Alabama, Tuscaloosa, AL, USA, in 2017. He developed several radar systems currently being used at KU for sounding and imaging of polar ice sheets. He has also participated in field experiments in the Arctic and Antarctica. He has authored or co-authored over 90 archival journal publications, 200 technical reports, and conference presentations. His current research interests include the application of radars to the remote sensing of the polar ice sheets, sea ice, ocean, atmosphere, and land.

Dr. Gogineni is a member of URSI, the American Geophysical Union, the International Glaciological Society, and the Remote Sensing and Photogrammetry Society. He was an Editor of the IEEE GEOSCIENCE AND REMOTE SENSING SOCIETY NEWSLETTER from 1994 to 1997.

**Jørgen Dall** (M'07) received the M.Sc. degree in electrical engineering and the Ph.D. degree from the Technical University of Denmark, Copenhagen, Denmark, in 1984 and 1989, respectively. He has been an Associate Professor since 1993. He has been working with the Danish airborne SAR, EMISAR, e.g. he led the development of onboard and offline SAR processors, was responsible for the data processing and organized the EMISAR data acquisition campaigns in a five year period. Later he led the development of the POLARIS sounder and SAR. His research interests include various aspects of ice sheet penetration, e.g. InSAR elevation bias, PolInSAR extinction coefficients, tomographic ice structure mapping, and ice sounding.